Computational and Theoretical Chemistry 998 (2012) 193–201

Contents lists available at SciVerse ScienceDirect

Computational and Theoretical Chemistry

journal homepage: www.elsevier.com/locate/comptc

Ionic interactions: Comparative topological approach

Julia Contreras-García [a,b,c,*], Mónica Calatayud [a,b,d], Jean-Philip Piquemal [a,b], J.M. Recio [c,e]

[a] UPMC Univ. Paris 06, UMR 7616, Laboratoire de Chimie Thorique, F-75005 Paris, France
[b] CNRS, UMR 7616, Laboratoire de Chimie Thorique, F-75005 Paris, France
[c] MALTA-Consolider Team, Spain
[d] Institut Universitaire de France, 103 bd Saint-Michel, 75005 Paris, France
[e] Dpto. de Química-Física y Analítica, Universidad de Oviedo, E-33006 Oviedo, Spain

ARTICLE INFO

Article history:
Received 20 May 2012
Received in revised form 18 July 2012
Accepted 18 July 2012
Available online 10 August 2012

Keywords:
Noncovalent interactions
Topological analysis
Ionic bonding
ELF
AIM
NCI

ABSTRACT

The NonCovalent Interaction (NCI) index applicability is extended to include ionic interactions, thus confirming its ability to detect both electronic and electrostatic effects. The characteristics of the reduced density gradient vs. the density, $s(\rho)$, and its isosurfaces are modeled thanks to the promolecular model, enabling to deeply understand the topological features of the function in ionic compounds. The analysis is extended to periodic systems in order to shed light into solid-state interactions. NCI reveals that anion–anion interactions contribute to crystal stability. These characteristics are compared to complementary functions, such as AIM and ELF, providing a quantitative framework for their comparison through the validity of the promolecular model. Shifts between nonhomeomorphic density and ELF topologies are shown to be related to the relative hardness of ions.

1. Introduction

Molecular structure is governed by covalent and noncovalent interactions. However, it is mainly noncovalent interactions that are the driving force in most biochemical processes. Chemical interactions between a protein and a drug, or a catalyst and its substrate, self-assembly of nanomaterials [1,2], and even some chemical reactions [3,4] are dominated by noncovalent interactions. These interactions include all interactions that are not due to electron sharing and they span a wide range of binding energies and encompasses hydrogen bonding, electrostatic interactions, steric repulsion, and London dispersion [5]. Noncovalent interactions might arise from two grounds: electronic (interference) or electrostatic (due to permanent or fluctuating charges).

More specifically, electrostatic interactions play a central role in a variety of biological processes. At any given pH, proteins have charged groups that may participate in binding, both in their folding and self-assembly and to other molecules. For example, negatively-charged carboxyl groups on aspartic acid (Asp) and glutamic acid (Glu) residues may be attracted by the positively-charged free amino groups on lysine (Lys) and arginine (Arg) residues. Electrostatic effects exert strongly stabilizing influences on cations, in many cases controlling the conformational preferences of these cations [6]. The lowest energy conformers are those where the positive charge is brought closest to substituents bearing partial negative charges. These conformational biases, along with stereoelectronic effects, can control the stereoselectivity of reactions involving carbo-cationic intermediates.

Noncovalent interactions, not being related directly to the molecular structure, but to its voids, still give rise to a vigorous debate about their presence and strength. Graphical visualization of macromolecular structures is having significant impact on the field of structure biology. Since electrostatic interactions are governed by the Coulomb law, these have most commonly been identified by distance analyses. However, this approach totally disregards electronic effects. It becomes thus interesting to be able to identify the existence of both electronic and electrostatic interactions which determine the protein structure and folding on a common ground.

We have recently developed a new approach, known as NCI (for NonCovalent Interactions), to detect noncovalent interactions in real space, based on the electron density and its derivatives [7]. It provides a rich representation of electronic effects such as van der Waals interactions, hydrogen bonds, and steric repulsion. Most importantly, the method, requiring only knowledge of the atomic coordinates, is efficient and applicable to large systems, such as proteins or DNA. Thus, the extension to include ionic interactions would be extremely appealing for the understanding of biomolecules. Along this article, the abilities of this tool will be taken one step further to include ionic bonding, thus covering the

* Corresponding author at: UPMC Univ. Paris 06, UMR 7616, Laboratoire de Chimie Thorique, F-75005 Paris, France.
E-mail address: contrera@lct.jussieu.fr (J. Contreras-García).

2210-271X/$ - see front matter © 2012 Elsevier B.V. All rights reserved.
http://dx.doi.org/10.1016/j.comptc.2012.07.043

whole range of noncovalent interactions (electronic and electrostatic) and introducing a holistic tool that can be applied even to large biosystems.

The paper is divided as follows. Firstly, we will give an overview of the topological tools that will be used along the article (AIM, ELF, NCI). In this framework, previous topological analyses (AIM, ELF) of ionic bonding will be introduced. Secondly, the computational details will be reviewed. In Section 4, we will (i) show how electrostatic interactions engross the list of interactions described by NCI, (ii) show the effects of periodicity in ionic crystals and (iii) establish a quantitative comparison between the AIM–ELF–NCI picture of ions and their radii. The paper ends with a summary of the most important findings along the paper.

2. Theoretical background

2.1. Topological analysis

Over the years, different approaches have been developed to understand chemical bonds. Molecular Orbital (MO) theory has been very useful and successful for the theoretical analysis of chemical reactions and chemical reactivity. The frontier orbital theory [8] and the orbital symmetry rules of Woodward and Hoffmann [9] are paradigmatic examples of the possibilities of quantum chemistry within the MO theory. To reduce the dimensionality of the problem, three dimensional interpretative approaches have been introduced. The conceptual density functional theory pioneered by Parr et al. [10] has been at the origin of very useful reactivity descriptors.

Another low dimensional approach has originally been developed by Bader [11]: the topological approach. The topological analysis relies on a partition of the molecular space achieved in the framework of the theory of gradient dynamics applied to a scalar potential function, say $V(\vec{r})$, which contains the physical or chemical information that we shall call "chemical potential function". Two types of topological information are obtained: local and global. Local information is gathered by evaluating density properties at distinctive points where the gradient vanishes. These points constitute a subset of special points of the field, named critical points (CPs), which contrary to wandering points ($\nabla V \neq 0$), may act as a source or a sink of more than one gradient path, depending on their nature. The number of nonzero eigenvalues of the Hessian, or rank, determines its dimensionality, and the sum of the signs of the Hessian eigenvalues characterizes the capability to receive or send gradient paths. In a stable 3D topology, this gives rise to the following possibilities: (3, −3) for local maxima or attractors, (3, +3) for local minima, and (3, −1) and (3, +1) for saddle points in one or two dimensions, respectively.

A region of space can be associated with each attractor or sink of the field. This partitioning gives rise to a set of nonoverlapping volumes or basins, Ω_i, whose boundaries or separatrices are zero-flux surfaces. Global information is acquired from volume integration of property densities over these spatial fragments. Most commonly, the integration of the density, ρ, over their volume, Ω_i, assigns a population, $\overline{N}$, to each basin:

$$\overline{V}(\Omega_i) = \int_{\Omega_i} d\vec{r} \tag{1}$$

$$\overline{N}(\Omega_i) = \int_{\Omega_i} \rho(\vec{r}) d\vec{r} \tag{2}$$

2.2. Chemical potential functions

Depending on the function used for the topological analysis, different partitions and pictures arise from the chemical system. Since the potential functions used in the partition have a chemical meaning, the global properties (charges and volumes) so obtained also have a chemical meaning. For example, integration of the density within the AIM framework provides atomic charges [11], whereas integration of the density within ELF regions [12,13] will yield information of the charge associated with bonds and lone pairs [14].

Three complementary chemical potential functions will be used along this article, which are summarized in Table 1.

2.2.1. The electronic density

In the Atoms In Molecules (AIMs) theory of Bader, the scalar function is the electron density distribution, whose basins have their attractors most commonly located on the nuclei and which are therefore associated with the atoms that constitute the molecule. According to Bader [11], the presence of a (3, −1) critical point of the density is a necessary condition for the two atoms to be bonded to one another when the system is in a stationary state (thus, (3, −1) critical points are called bond critical points within this framework).

The example in Table 1 shows the ability of AIM to identify the bonds in benzene dimer, both inter and intramolecular. Bond critical points (red) appear in between covalently bonded C—C and C—H pairs and for the intermolecular weak interactions. Ring critical points (yellow) appear associated with the benzene ring as well as with the intermolecular interaction. As we will see, these ring critical points will also be critical points in the NCI topology. However, the fact that interactions are related to saddle points, locates them on the interatomic surfaces, so that they highlight interatomic contact, but they do not have an associated region within this approach.

2.2.2. The kinetic energy density

In order to recover a chemist's representation of a molecule consistent with Lewis' valence picture, one must use another local function that is able to describe the electron pair regions. The

Table 1
Comparison between AIM, ELF and NCI topologies in benzene dimer.

Method	AIM	ELF	NCI
Function	Electron density	Pauli kinetic energy density	Reduced density gradient
Partition	Atoms	Lewis' pairs	Noncovalent interactions
Example	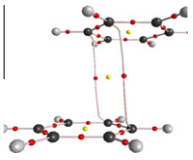	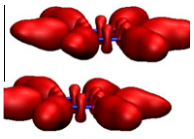 ELF=0.9	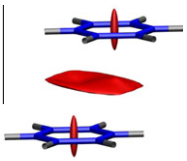 s=0.6, $\rho < 0.05$

electron localization function, η, was originally designed by Becke and Edgecombe to identify "localized electronic groups in atomic and molecular systems" [15]. As interpreted by Savin et al. [16], the ELF core, χ, can be understood as a local measure of the excess of local kinetic energy of electrons due to the Pauli principle, t_p:

$$\chi_\sigma(\mathbf{r}) = \frac{t_p(\vec{r})}{t_{HEG}(\vec{r})} \tag{3}$$

in which t_p is the difference between the definite positive kinetic energy $t(\vec{r})$ and the von Weizsäcker kinetic energy functional:

$$t_p(\vec{r}) = t(\vec{r}) - \frac{1}{4}\frac{|\rho_\sigma(\vec{r})|^2}{\rho_\sigma(\vec{r})} \tag{4}$$

and $t_{HEG}(\vec{r}) = \frac{3}{5}(6\pi^2)^{2/3}\rho_\sigma^{5/3}(\vec{r})$ is the kinetic energy density of the homogeneous electron gas.

ELF values are confined in the [0,1] range by a Lorentzian transformation which facilitates its interpretation:

$$\eta = \frac{1}{1+\chi^2} \tag{5}$$

ELF basins appear associated with localized electron pairs, such as bonds, lone pairs and atomic shells, thus matching the VSEPR model. As for noncovalent interactions, changes are observed in the ELF value at the first order saddle point [17,18]. This approach, known as EDI (ELF Delocalization Index), enables to understand bond formation and delocalization from one electron properties. However, due to the lack of electronic localization in most noncovalent interactions, this approach is not able to visualize weak interactions. As can be seen in Table 1, the VSEPR regions of benzene dimer are clearly identified by ELF, but nothing is seen for the inter benzene stacking interaction.

2.2.3. The reduced density gradient

NCI is a visualization index based on the analysis of the reduced density gradient, s, at low densities [7,19]:

$$s = \frac{1}{c_F}\frac{|\nabla\rho|}{\rho^{4/3}} \tag{6}$$

where $c_F = 2(3\pi^2)^{1/3}$ is the Fermi constant and the 4/3 exponent in the density ensures that s is a dimensionless quantity. Fig. 1 shows the reduced density gradient vs. electron density for formic acid (Fig. 1a) and formic acid dimer (Fig. 1b). These graphs have been obtained thanks to the `NCIPLOT` code written by some of the authors [19]. This code constructs a grid over the molecular space, analyzing ρ and s point-wise, which enables reconstructing the reduced density gradient behavior as shown in Fig. 1. This representation shows characteristic peaks at low density in the presence of noncovalent interactions due to the annihilation of the density gradient at these points (Fig. 1b).

The isosurfaces that encompass these interaction-peaks contour the noncovalent interactions in the system, both favorable and unfavorable. As an example, Table 1 shows both the steric repulsion associated with the ring tension and the attractive dispersive interaction between the benzene monomers. In order to differentiate between these different types of interactions, the sign of the second density Hessian eigenvalue times the density is used. This value is able to characterize the strength of the interaction by means of the density, and its character thanks to the sign of the second eigenvalue.

The method is applicable to small molecules as well as inorganic complexes. Furthermore, the method is also applicable to promolecular densities, enabling the analysis of biomolecules.

2.3. Ionic bonding – topological approach background

Probably the simplest and earliest proposed classification of bonding within the theory of atoms in molecules [11] is that based on the sign of the Laplacian at the bond critical point, $\nabla^2\rho_{(3,-1)} = \lambda_1 + \lambda_2 + \lambda_3$, where λ_i are the main curvatures. Since $\lambda_3 \geqslant \lambda_2 \geqslant \lambda_1$, at the bond critical point $\lambda_3 > 0$ and λ_2, $\lambda_1 < 0$. Generally, shared chemical interactions (covalent and polar bonds) are characterized by negative $\nabla^2\rho_{(3,-1)}$ values and hence dominant negative curvatures, with lowering of the potential energy arising from the charge being concentrated between the nuclei along the bond path. Conversely, closed-shell interactions (ionic bonds, hydrogen bonds, van der Waals interactions) have positive $\nabla^2\rho_{(3,-1)}$ values and hence a dominant positive λ_3 curvature, with their energetic stability being attained from the electronic charge that is concentrated within the atomic basins, rather than being shared between them. Closed-shell interactions are characterized by relatively low values of $\rho_{(3,-1)}$ because the density is contracting away from the interatomic surface in requirement to the Pauli exclusion principle. In the case of ionic interactions a further charge transfer is observed after integration of the corresponding basins [20].

It should be noted that ionicity is most clearly observed in the solid state, thanks to the stabilization of charges throughout the periodic network. Within the framework of the topology of the electron density, an in-depth comprehensive analysis of ionic crystals has been carried out by Luaña et al. [21] and Martín Pendás et al. [22,23].

Although the AIM approach enables to settle the strength of an ionic bond, it does not provide insight into the bonding in terms of electronic pairing within the crystal. The ELF function provides further insight in this direction. From the advent of the visual ELF

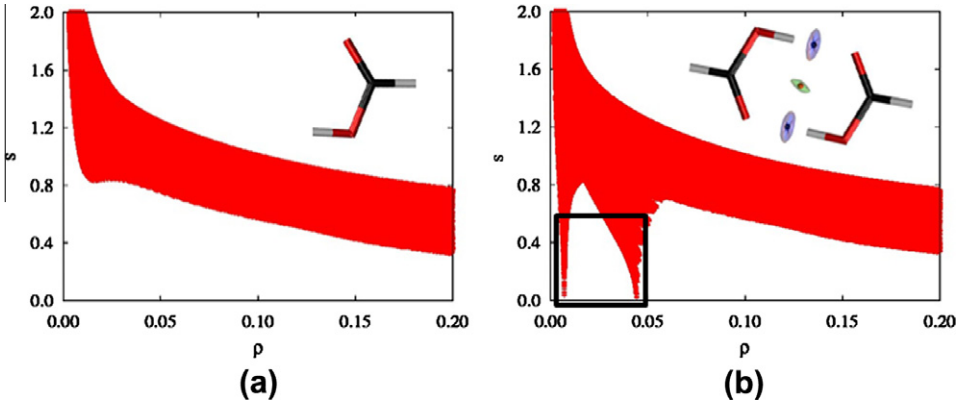

Fig. 1. NCI analysis in the formation of formic acid dimer. (a) $s(\rho)$ for formic acid and (b) $s(\rho)$ for formic acid dimer. NCI isosurfaces are shown in the insets for $s = 0.6$ au and colored according to a BGR scheme over the range $-0.04 < sign(\lambda_2)\rho < 0.4$ a.u. Critical points of the density have been included for comparison and are colored according to their signature: (3, −1) = black, (3, +1) = red. (For interpretation of the references to color in this figure legend, the reader is referred to the web version of this article.)

analysis [24], it was recognized that ionic compounds were identified within this framework by a closed-shell electrostatic interaction between ions, which in the ELF picture involves the lack of bonding basins, only showing closed-shell basins whose shape approach that of a sphere [25].

Indeed, due to the absence of bonding basins, not much attention was paid initially to the topological analysis of ELF in ionic crystals. This gap was even deeper in solids, where the computational complexity of the localization of all the critical points refrained its full exploitation. Thanks to a code [26,27] that some of the authors have recently implemented, these difficulties have been overcome, enabling determination of bond formation and delocalization between basins by means of the analysis of ELF (3, −1) critical points [17,18]. As far as ionic interactions are concerned, a comprehensive and quantitative description of ionic solids within the ELF framework has been recently introduced, showing how coordination and phase transitions can be tracked by the means of the complete determination of the ELF topology [25,28,29].

3. Computational details

To obtain plots of the electron density and reduced density gradient density-functional in molecules calculations were performed with the B3LYP functional [30,31] and the 6-31G* basis set, using the Gaussian 09 program [32]. Molecular geometries were optimized at the same level through the Berny algorithm [32,33]. Plots of s vs. ρ were obtained thanks to the `NCIPLOT` program developed by some of the authors [19,34] with grids of 0.1 Å along each axis.

In solids, crystalline wavefunctions have been obtained for the B1 phase of the AX (A: Li, Na, K; X: F, Cl, Br) alkali halide family within the density functional theory framework under the generalized gradient approximation with Becke [35] exchange and PW91 correlation [36] functionals as implemented in the `CRYSTAL98` code [37]. Basis sets have been taken from literature sources [38,39] and unit cell parameters set to the experimental values of the stable rock-salt structures at room temperature conditions [23].

AIM, ELF and NCI visualization for solids has been implemented in a second version of the critic code [40], which can use density information from `Quantum ESPRESSO` [41], `abinit` [42,43], `VASP` [44,45], `WIEN2k` [46,47], `elk` [48] or `pi7` [49] as input. In addition, `critic2` reads density cubes in `Gaussian` [32] and `XCrysden` [50] formats, so any program not directly supported can be interfaced with `critic2` via density grids.

4. Results and discussion

4.1. Ionic bonding within NCI

The following set of ionic molecules have been analyzed LiX, NaX and KX, with X = F, Cl. Results are collected in Figs. 2–4. Several common characteristics arise: two different decaying curves are observed at different height (some with a change in slope at medium densities), and a set of two nearly symmetrical peaks.

Densities in ionic crystals are almost nonoverlapping, thus they are well described by promolecular densities [23]. Atomic/ionic densities can be modeled by exponential basis functions for each shell [51,52]:

$$\rho_{at}^{prom} = \sum_n c_n e^{\zeta_n r} \tag{7}$$

where n stands for the number of shells. In the region of the interaction, this reduces to the valence (i.e. the outermost shell), so that the density for an ionic pair AB at a mutual distance R is given by:

$$\rho(r) = \rho_A^{prom} + \rho_B^{prom} = ae^{-\alpha r} + be^{-\beta(R-r)} \tag{8}$$

where a, α, b and β are positive constants characteristic of the A and B ions, respectively [23].

For r close to A, we can assume that $\rho(r) \simeq \rho_A(r) = a\ e^{-\alpha r}$, and analogously for r close to B. In those cases, the reduced density gradient reduces to the free-ion behavior:

$$s(r \to r_A) = \alpha a e^{-\alpha r/3} = \alpha \rho^{-1/3} \tag{9}$$

Thus, these regions give rise to two curves of a $y = cx^{-1/3}$ exponential behavior, where the constant c, determines the displacement of the curve along the y axis. The exponential constants α and β are associated with the difficulty to deform, or hardness, of the ions [23]. Thus, the relative position of the curves can be associated with the relative hardness of the ions.

Since cations are generally harder than anions, i.e. $\alpha > \beta$, in most cases the cation curve will be over the anionic line at low (valence) densities. This is exactly what is observed in LiX (Fig. 2 top) and NaX (Fig. 3 top), with X = F, Cl. Two decaying curves, one for each ion, with the cation on top of the anion by $\alpha - \beta$. However, for potassium salts, the cation contribution is softer, yielding even to an inversion for KF (Fig. 4 left), where the anionic F^- curve is over the K^+ line at low densities. Indeed, the similar hardness of K^+ and F^- was already observed within the AIM [23] and ELF [25] topologies.

This provides us with an easy to visualize way to recognize cation–anion contributions to the $s(\rho)$ plot as well as to cast the relative hardness of the ions: the greater the difference between the curves, the greater the ionic hardness difference between them.

In the case of third row elements (K, Cl) a sudden change in slope is observed at medium densities. This fact can be easily understood by means of our promolecular model (Eq. (7)). These densities lack relaxation, but since the overalp in ionic crystals is very small, it can also be used to understand the behavior of the $s(\rho)$ curve at the atomic level.

Fig. 5 shows the promolecular model for the chlorine density with the slope change observed in Figs. 2–4 highlighted in the inset. Parameters have been taken from Ref. [7]. When we analyze the behavior of each shell contribution, it comes out clear that the change in slope is associated with a change from one shell to another with a different characteristic hardness (ζ_n exponent).

Finally, the appearance of peaks is directly related to the existence of density (3, −1) critical points between the ions. When the density gradient is zero, $s(\rho)$ becomes zero too (see Eq. (6)). Since $s \geqslant 0$, the critical points of the density are minima of the reduced density gradient. The ionic bond critical point induces a crucial change in the reduced density gradient between the ions involved. Since the behavior of s at low densities is dominated by $\rho \to 0$, it tends to ∞ except in the regions around a density critical point, where $\nabla\rho \to 0$ dominates, giving rise to a steep peak that goes to zero. The neighboring points of the density bond points show the same signature as the (3, −1) critical point itself, giving rise to a negative second eigenvalue. However, as was already observed in hydrogen bonds [53], the region surrounding the critical point shows the electronic repulsion induced by the density overlap, giving rise to $\lambda_2 > 0$. This is why two peaks are observed in the top Figs. 2–4: one for $\lambda_2 > 0$ and another one for $\lambda_2 < 0$.

The cutoff used in the representation of NCI isosurfaces will determine which features are observed. Due to the ionic critical points present in our systems, these noncovalent interactions will be observed from the beginning (Figs. 2–4 bottom left). Disc-shaped isosurfaces appear in between the ions that represent the ionic bond. Thus, NCI is able to reveal all types of noncovalent bonds, be them electronic or electrostatic in origin. The size of the isosurfaces will be greater for fluorides than for chlorides, due to the fact that the peaks for the former have a greater surface than the latter. The coloring of the surface, determined by the density, will be related to the strength of the interaction.

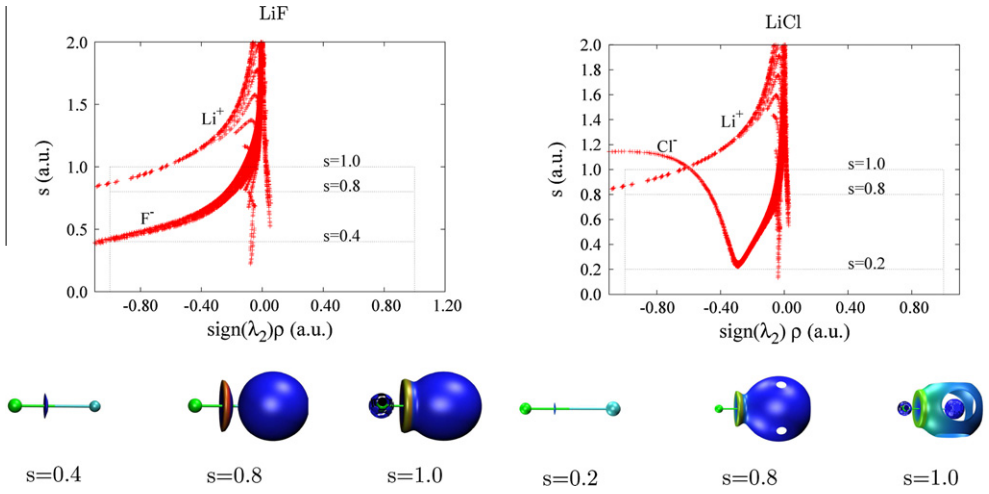

Fig. 2. NCI for LiF (left) and LiCl (right). Top: $s(\rho)$, bottom: NCI isosurfaces for various cutoffs (indicated below each figure). The part of the $s(\rho)$ diagram covered by each isosurface is highlighted in the $s(\rho)$ plot by the corresponding frames.

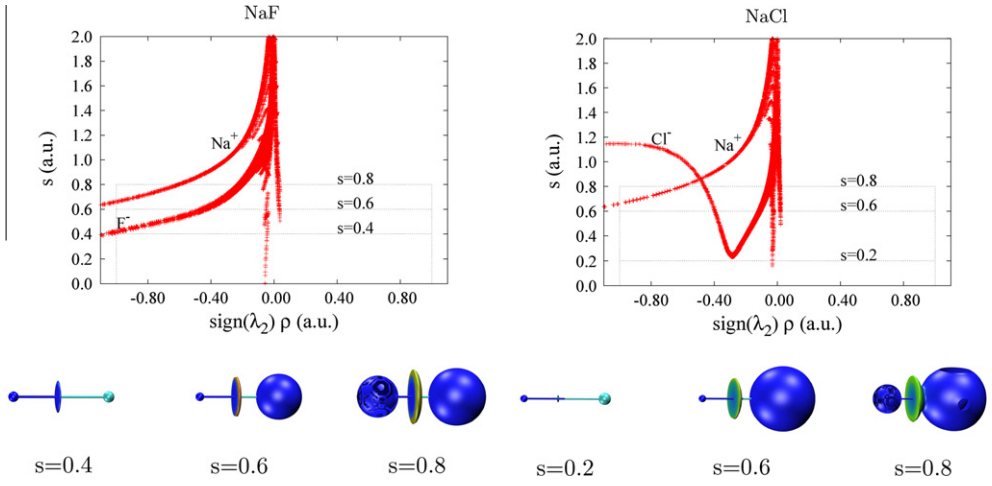

Fig. 3. NCI for NaF (left) and NaCl (right). Top: $s(\rho)$, bottom: NCI isosurfaces for various cutoffs (indicated below each figure). The part of the $s(\rho)$ diagram covered by each isosurface is highlighted in the $s(\rho)$ plot by the corresponding frames.

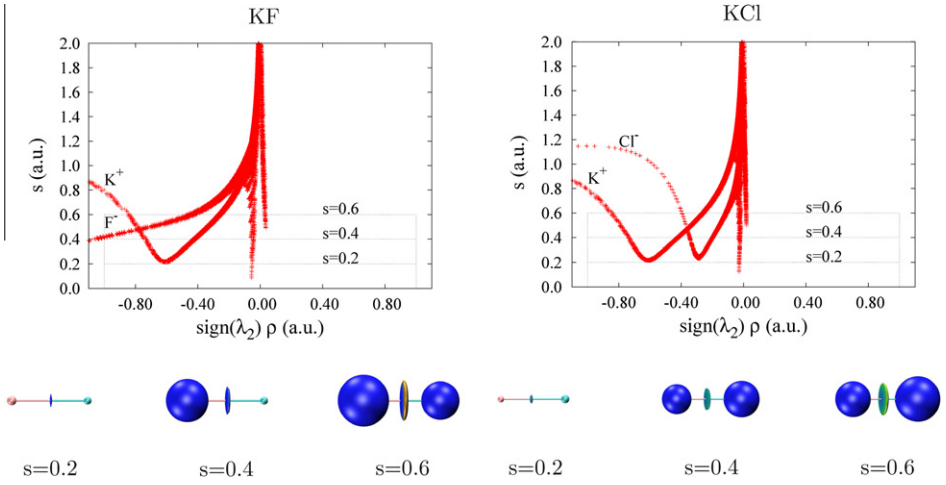

Fig. 4. NCI for KF (left) and KCl (right). Top: $s(\rho)$, bottom: NCI isosurfaces for various cutoffs (indicated below each figure). The part of the $s(\rho)$ diagram covered by each isosurface is highlighted in the $s(\rho)$ plot by the corresponding frames.

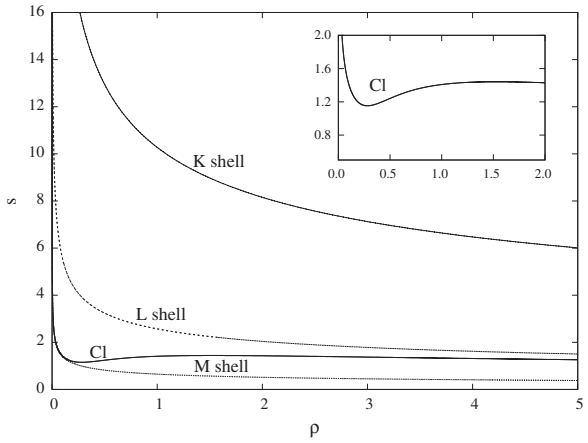

Fig. 5. Promolecular model for Cl atom. Each shell is represented by an exponential as in Eq. (7), yielding three shell lines (K, L, M) for chlorine. The slope change observed in the ionic plots is highlighted in the inset. It is due to the fact that those densities are mainly dominated by the L shell and not anymore by the M shell.

The presence of repulsive areas in the NCI ionic interaction is visualized at greater cutoffs, when the region around the critical point is included. In the fluorides, where the density is stronger, the repulsion is easily seen as a red circle surrounding the bonding area. However, for greater anions, this repulsion is smaller, and only green surfaces are observed.

4.2. Ionic interactions in crystals

There are several factors that draw a clear line between the molecular and the crystalline realms as far as the study of their topology is concerned. On the one hand, and due to the periodicity of the solid, an infinite number of critical points is expected [22].

Furthermore, for a periodic system, the Morse relationship that holds reads as follows:

$$n_{(3,-3)} - n_{(3,-1)} + n_{(3,+1)} - n_{(3,+3)} = 0 \tag{10}$$

being n the number of critical points of a given type. The existence of (3, +3) points is ensured by the Weierstrass theorem, which accordingly enforces the presence of the whole set of types of critical points of rank 3 within the following lower limits:

$$n_{(3,-3)} \geqslant 1, \quad n_{(3,-1)} \geqslant 3, \quad n_{(3,+1)} \geqslant 3, \quad n_{(3,+3)} \geqslant 1 \tag{11}$$

Fig. 6 shows how NCI behaves in a simple crystal (fcc-NaCl). It can be seen that the main $s(\rho)$ characteristics are preserved from the molecular realm. However, two slight differences appear, which are consistent with the known real-space features of the electron density.

Firstly, the $s(\rho)$ plot becomes thinner. This is due to the highly symmetric pattern of the periodic density in the B1 phase. Secondly, new interactions appear related to the fact that all types of critical points should be present. These appear of course at lower densities, giving rise to a continuous transition between the attractive and repulsive cation–anion peaks. These interactions are related to dispersive interactions within the crystal, but most importantly to the anion–anion interactions (see Fig. 6) that were already observed both within the AIM [23] and the ELF [25] frameworks. Indeed, the occurrence of bonding interactions in a crystal between like-charged species that contribute significantly to the crystal packing formation has long been analyzed [23,25,54] and is now confirmed by NCI analysis. The strongest interaction in terms of electron density at the NCI domain is still the cation–anion contact.

4.3. Quantitative comparative topological approach to ionic bonding

The aim of this final subsection is to study the topological radii resulting from the AIM, ELF and NCI analysis of the alkali halides. Ionic radii have played a determinant role in solid state physics as the main structural parameter available to systematize crystal properties [55]. For a long time these distances were considered as the contact radii between spheres, regardless of the obvious drawbacks this hypothesis had. On the one hand, it is necessary to split the inter-nuclear distance of adjacent atoms into contributions of different species. This requires an initial assignment of a reference radius for the construction of a congruent set of data. On the other hand, the spherical atomic volumes calculated from these radii do not reconstruct the cell volume. These two shortcomings are overcome when topological radii are used, since they are rigorously defined, and being direction dependant, they fill up the whole space. It is interesting to note that nonspherical ions is the actual picture provided by experiments: recent measurements of accurate electron densities have proved that an ion may display different radii along different directions [56].

Bader's theory of atoms in molecules [11] provides an unambiguous framework in which to assign an accurate meaning to geometric coordinates in solids. In a condensed phase, an AIM-defined atom (or ion) is a closed region of the physical space, having well-defined boundaries and volume. The location of the ionic bond critical point between cations and anions allows defining both cationic and anionc radii within the crystal. In Section 4.1, we have seen that all critical points of AIM constitute minima of the NCI topology. Thus, the definition of ionic radii within both topologies is equivalent. This is however not the case of ELF, whose topology has been shown to be nonhomeomorphic with the density [57]. Within the ELF framework, the absence of bonding basins in ionic

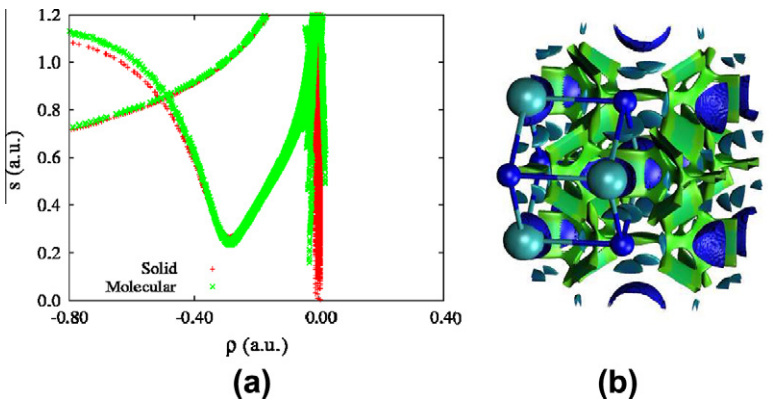

Fig. 6. NCI for solid NaCl. (a) $s(\rho)$ For solid (red) and molecular (green) NaCl and (b) NCI isosurface for s = 0.5. (For interpretation of the references to color in this figure legend, the reader is referred to the web version of this article.)

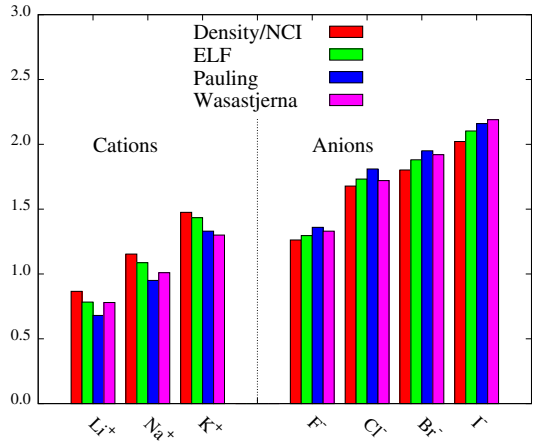

Fig. 7. Ionic radii in the alkalihalides according to ELF, Wasastjerna [58], Pauling [59] and QTAIM [23]. Atomic radii are also provided for comparison (Å).

systems enables to define ionic superbasins as the sum of core and valence shells belonging to the same ion. This allows the partition of the crystal into ions, whose radii are determined by the position of the (3, −1) points along the cation–anion interaction line.

In order to quantitatively compare these topologies, density and ELF radii have been taken from the literature (see Ref. [25] for computational details) for the B1 phase of the AX (A: Li, Na, K; X: F, Cl, Br) alkali halide family. Results are collected in Fig. 7, along with empirical radii. Topological radii are compared with two empirical sets of radii: Wasastjerna's [58] and Pauling's [59]. The former were determined from polarizabilities, whereas the latter are inversely proportional to the effective nuclear charge.

We can see that topologically-determined radii follow very well the overall empirical trends both in anions and cations (Fig. 7). However, a clear slight deviation arises. In both density and ELF topologies, anions are slightly smaller and cations are slightly bigger. As already noted before [25], this deviation is more pronounced in the case of the AIM approach, with ELF radii always matching closer the experimental values.

The promolecular model previously introduced can be used to understand the relationship between the different sets of topological radii. For that, we need to study the location of the points where the gradient of the density and the ELF annihilate along the bonding line: $\vec{r}_\rho$ where $\nabla\rho(\vec{r}_\rho) = 0$ and $\vec{r}_\eta$ where $\nabla\eta(\vec{r}_\eta) = 0$, respectively. Since the actual formulation of ELF is a mapping of its core χ (Eq. (5)), it is only necessary to find the critical points associated to this simpler function. Furthermore, since ions are nearly spherical, we will only consider the main contribution, that is, radial derivatives. Going back to Eq. (3), the ELF or χ radius is determined by the following condition:

$$\left.\frac{d\chi(r)}{dr}\right|_{r_\eta} = \frac{dt_p(r)}{c_F\rho^{5/3}(r)} - \frac{5}{3}\frac{d\rho(r)t_p}{c_F\rho^{8/3}(r)} = 0 \tag{12}$$

After rearranging the terms we have:

$$\frac{dt_p(r)}{t_P(r)} - \frac{5}{3}\frac{d\rho(r)}{\rho(r)} = 0 \tag{13}$$

where the first term, which we shall call $Y_1(r) = d\,t_p(r)/t_P(r)$ depends only on the kinetic energy density and its derivatives, and the second one, which we shall call $Y_2(r) = 5d\rho(r)/3\rho(r)$ depends only on the electronic density and its derivatives. This arrangement is especially interesting for relating the position of the density and ELF critical points from the condition $Y = Y_1 - Y_2 = 0$.

Fig. 8 shows the behavior of Y_1, Y_2 and Y for LiF, with Li^+ standing on the left and F^- on the right of the plot. The behavior of $Y_2(r)$ can be understood from the promolecular model. From Eq. (8) we can see that the density gradient and the Laplacian are given by:

$$\nabla\rho(r) = -\alpha a e^{-\alpha r} + \beta b e^{-\beta(R-r)} \tag{14}$$

$$\nabla^2\rho(r) = \alpha^2 a e^{-\alpha r} + \beta^2 b e^{-\beta(R-r)} > 0 \tag{15}$$

Since a, α, b and β are positive, the Laplacian is positive everywhere and $\nabla\rho$ and Y_2 are increasing functions in ionic crystals which annihilate at the AIM critical point.

The position of the ELF critical point is hence shifted due to $Y_1(r) = dt_P(r)/t_P(r)$. The sign of this contribution determines whether the shift takes place toward the cation or the anion. From its definition the Pauli kinetic energy density, t_P, is positive. This can be seen in Fig. 8b, where we also see that t_p increases toward the cation, yielding $dt_p < 0$ in our case (cation is on the right). Indeed, the sign of dt_P can be deduced assuming that each ionic tail wavefunction can be reduced to one exponential $e^{-\alpha r/2} = \rho_A^{1/2}$ and that close to the critical point, $\nabla\rho(r) \simeq 0$, so that $t_p \simeq t$, with:

$$dt = \frac{\alpha^3 a}{16}e^{-\alpha r/2} - \frac{\beta^3 b}{16}e^{-\beta(R-r)/2} = \alpha^3\rho_A^{1/2} - \beta^3\rho_B^{1/2} < 0 \tag{16}$$

where we have made use of the fact that most generally $\alpha > \beta$, so that both dt and dt_p are negative in our ionic arrangement. It follows that the kinetic energy density increases toward the harder ion as seen in Fig. 8b. Therefore, Y_1 is negative and shifts the curve toward the cation, thus explaining the fact that the ELF cationic radii be smaller than the AIM and NCI ones.

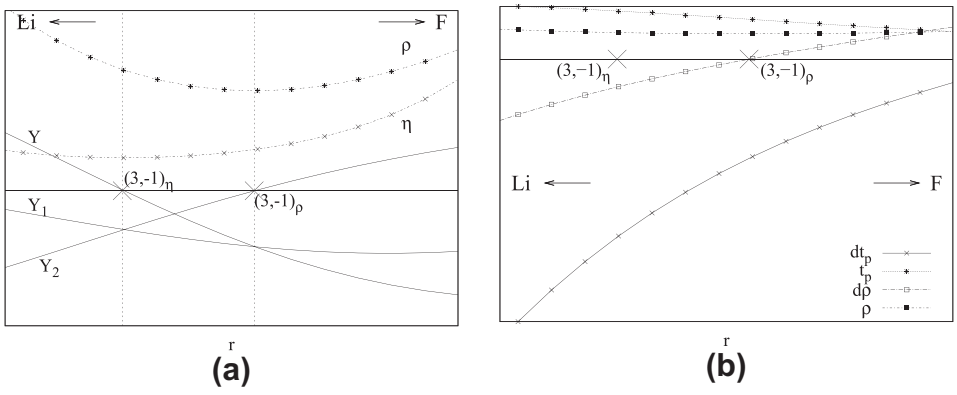

Fig. 8. Decomposition of density and kinetic energy density terms of LiF around ELF, AIM and NCI critical points. Li lies on the left and F on the right. Values of ρ and ELF have been rescaled for a clearer view. Meaning of symbols as in the text.

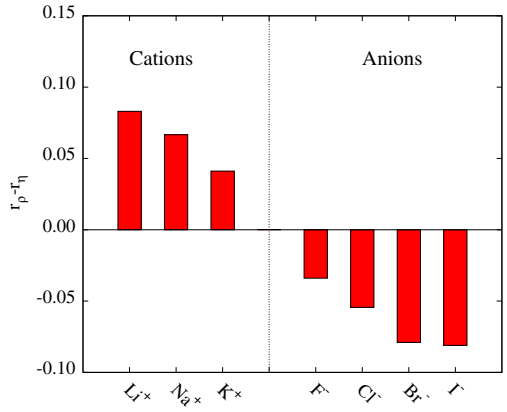

Fig. 9. Difference between AIM and ELF radii in Å for cations and anions in the alkalihalide family

Fig. 8 illustrates how $Y_1(r)$ stays negative along the whole interacting region for LiF, giving rise to a shift of $Y(r)$ toward the cation. Hence, the ELF critical point, where $Y_1(r) = Y_2(r)$ arises closer to the latter.

It is important to note that there has always been a big concern in understanding the relationship between the topology induced by ELF and that induced by the electron density. Resorting to ionic topologies, where all chemical quantities are well defined (ions), has enabled us to settle a quantitative comparison of these topologies, shedding light to the fact that the relative hardness of ions is responsible for the shift between ELF and AIM critical points. Indeed, greater differences are observed for harder cations (see Li^+ in Fig. 9) and softer anions (see Cl^- and Br^- in Fig. 9).

5. Conclusions

Graphical visualization of macromolecular structures is having significant impact on the field of structure biology. Since electrostatic interactions are governed by the Coulomb law, these have most commonly been identified by distance analyses. However, this approach totally disregards electronic effects.

Along this contribution, we have settled the basis for a combined analysis of electrostatic and electronic noncovalent interactions in terms of the noncovalent interaction index. The applicability of this index, used up to now only for electronic effects, has thus been enlarged to include ionic interactions. The behavior of this index in ionic compounds has been well characterized: the behavior of atomic tails has been analyzed in terms of the promolecular model and the peaks have been put in relationship with the AIM topology. The applicability of NCI to large biosystems, along with its ability to describe electronic and electrostatic effects will be the subject of a future contribution in which protein interactions will be analyzed.

A new code for crystalline systems has been used in order to establish the differences introduced by periodicity. The existence of anion–anion interactions has been confirmed from the NCI point of view as contributing (though less than direct contacts) to crystal stability.

Finally, a new step has been taken in the understanding of the relationship between the topologies induced by different chemical potential functions. Along this contribution, ionic compounds have been used as a prototypical example where both ELF and AIM topologies should yield similar results. The shift between the two has been quantitatively related to the relative hardness of the ions involved, thus settling a first step for the quantitative understanding of the relationship between nonhomeomorphic topologies.

Acknowledgments

Financial and computational support from the MALTA-Consolider Ingenio-2010 program under Project CSD2007-00045 is acknowledged. JCG thanks the Spanish Ministry of Education for a postdoctoral Grant (Orden EDU/2253/2010). JMR thanks the Spanish Ministry of Education for financial support (CTQ2009-14596-C02-02).

References

[1] H. Fenniri, M. Packiarajan, K.L. Vidale, D.M. Sherman, K. Hallenga, K.V. Wood, J.G. Stowell, Helical rosette nanotubes: design, self-assembly, and characterization, J. Am. Chem. Soc. 123 (2001) 3854–3855.
[2] P. Kruse, E.R. Johnson, G.A. DiLabio, R.A. Wolkow, Patterning of vinylferrocene on HSi(100) via self-directed growth of molecular lines and STM-induced decomposition, Nano Lett. 2 (2002) 807–810.
[3] S.S. Sheiko, F.C. Sun, A. Randall, D. Shirvanyants, M. Rubinstein, H. Lee, K. Matyjaszewski, Adsorption-induced scission of carboncarbon bonds, Nature. 440 (2006) 191–194.
[4] G.A. DiLabio, P.G. Piva, P. Kruse, R.A. Wolkow, Dispersion interactions enable the self-directed growth of linear alkane nanostructures covalently bound to silicon, J. Am. Chem. Soc. 126 (2004) 16048–16050.
[5] P.A. Kollman, Recent progress in stereochemistry, Chem. Rev. 10 (1977) 365–426.
[6] D.M. Smith, K.A. Woerpel, Electrostatic interactions in cations and their importance in biology and chemistry, Org. Biomol. Chem. 4 (2006) 1195–1201.
[7] E.R. Johnson, S. Keinan, P. Mori-Sánchez, J. Contreras-García, A.J. Cohen, W. Yang, Revealing noncovalent interactions, J. Am. Chem. Soc. 132 (2010) 6498–6506.
[8] K. Fukui, T. Yonezawa, H. Shinghu, A molecular orbital theory of reactivity in aromatic hydrocarbons, J. Chem. Phys. 20 (1952) 722–725.
[9] R.B. Woodward, R. Hoffmann, The conservation of orbital symmetry, Angew. Chem. Int. Ed. Engl. 8 (1969) 781–853.
[10] R.G. Parr, R.A. Donnelly, M. Levy, W.E. Palke, Electronegativity: the density functional viewpoint, J. Chem. Phys. 68 (1978) 3801–3807.
[11] R.F.W. Bader, Atoms in Molecules: A. Quantum Theory, Oxford University Press, Oxford, 1990.
[12] B. Silvi, A. Savin, Classification of chemical bonds based on topological analysis of electron localization functions, Nature 371 (1994) 683–686.
[13] U. Häussermann, S. Wengert, R. Nesper, Localization of electrons in intermetallic phases containing aluminum, Angew. Chem. Int. Ed. Engl. 33 (1994) 2069–2073.
[14] M. Kohout, Atomic shell structure and electron numbers, Int. J. Quantum Chem. 60 (1996) 875–882.
[15] A.D. Becke, K.E. Edgecombe, A simple measure of electron localization in atomic and molecular systems, J. Chem. Phys. 92 (1990) 5397–5403.
[16] A. Savin, O. Jepsen, J. Flad, L.K. Andersen, H. Preuss, H.G. von Schnering, Electron localization in solid-state structures of the elements: the diamond structure, Angew. Chem. Int. Ed. Engl. 31 (1992) 187–188.
[17] J. Contreras-García, J.M. Recio, Electron delocalization and bond formation under the ELF framework, Theor. Chem. Acc. 128 (2011) 411–418.
[18] J. Contreras-García, A. Martín Pendás, B. Silvi, J.M. Recio, Bases for understanding polymerization under pressure: the practical case of CO_2, J. Phys. Chem. B. 113 (2009) 1068–1073.
[19] J. Contreras-García, E.R. Johnson, S. Keinan, R. Chaudret, J-P. Piquemal, D. Beratan, W. Yang, NCIPLOT: a program for plotting noncovalent interaction regions, J. Chem. Theory Comput. 7 (2011) 625–632.
[20] P. Mori-Sánchez, A. Martín Pendás, V. Luaña, A classification of covalent, ionic, and metallic solids based on the electron density, J. Am. Chem. Soc. 124 (2002) 14721–14723.
[21] V. Luaña, A. Costales, A. Martín Pendás, Ions in crystals: the topology of the electron density in ionic materials. II. The cubic alkali halide perovskites, Phys. Rev. B 55 (1997) 4285–4297.
[22] A. Martín Pendás, A. Costales, V. Luaña, Ions in crystals: the topology of the electron density in ionic materials. I. Fundamentals, Phys. Rev. B 55 (1997) 4275–4284.
[23] A. Martín Pendás, A. Costales, V. Luaña, Ions in crystals: the topology of the electron density in ionic materials. III. Geometry and ionic radii, J. Phys. Chem. B 102 (1998) 6937–6948.
[24] A. Savin, R. Nesper, S. Wengert, T.F. Fässler, ELF: the electron localization function, Angew. Chem. Int. Ed. Engl. 36 (1997) 1808–1832.
[25] J. Contreras-García, J.M. Recio, On bonding in ionic crystals, J. Phys. Chem. C. 115 (2011) 257–263.
[26] J. Contreras-García, A. Martín Pendás, B. Silvi, J.M. Recio, Useful applications of the electron localization function in high-pressure crystal chemistry, J. Phys. Chem. Solids 69 (2008) 2204–2207.
[27] J. Contreras-García, A. Martín Pendás, B. Silvi, J.M. Recio, Computation of local and global properties of the electron localization function topology in crystals, J. Theor. Chem. Comp. 5 (2009) 164–173.

[28] J. Contreras-García, A. Martín Pendás, B. Silvi, J.M. Recio, How electron localization function quantifies and pictures chemical changes in a solid: the B3 → B1 pressure induced phase transition in BeO, J. Phys. Chem. B. 112 (2008) 9787–9794.
[29] J. Contreras-García, P. Mori-Sánchez, B. Silvi, J.M. Recio, A quantum chemical interpretation of compressibility in solids, J. Chem. Theor. Comp. 5 (2009) 2108–2114.
[30] A.D. Becke, Density functional thermochemistry. III. The role of exact exchange, J. Chem. Phys. 98 (1993) 5648–5652.
[31] C. Lee, W. Yang, R.G. Parr, Development of the Colle–Salvetti correlation-energy formula into a functional of the electron density, Phys. Rev. B. 37 (1988) 785–789.
[32] M.J. Frisch et al., Gaussian 09 Revision A.1, Gaussian Inc. Wallingford CT, 2009.
[33] H.B. Schlegel, Optimization of equilibrium geometries and transition structures, J. Comput. Chem. 3 (1982) 214–218.
[34] http://www.chem.duke.edu/yang/Software/softwareNCI.html.
[35] A.D. Becke, Density-functional exchange-energy approximation with correct asymptotic behavior, Phys. Rev. A 38 (1988) 3098–3100.
[36] J.P. Perdew, Unified Theory of Exchange and Correlation Beyond the Local Density Approximation, Akademishe Verlag, Berlin, 1991.
[37] V.R. Saunders, R. Dovesi, C. Roetti, M. Causá, N.M. Harrison, R. Orlando, C. Zicovich-Wilson, CRYSTAL98 User's Manual, University of Torino, Torino, 1998.
[38] http://www.tcm.phy.cam.ac.uk/mdt26/crystal.html.
[39] M. Prencipe, A. Zupan, R. Dovesi, E. Aprá, V.R. Saunders, Ab initio study of the structural properties of LiF, NaF, KF, LiCl, NaCl, and KCl, Phys. Rev. B 51 (1995) 3391–3396.
[40] A. Otero-de-la-Roza, J. Contreras-Garca, E.R. Johnson, Revealing non-covalent interactions in solids: NCI plots revisited. Phys. Chem. Chem. Phys. 14 (2012) 12165–12172.
[41] P. Giannozzi, S. Baroni, N. Bonini, M. Calandra, R. Car, C. Cavazzoni, D. Ceresoli, G. Chiarotti, M. Cococcioni, I. Dabo, et al., QUANTUM ESPRESSO: a modular and open-source software project for quantum simulations of materials, J. Phys.: Condens. Matter 21 (2009) 395502.
[42] X. Gonze, J. Beuken, R. Caracas, F. Detraux, M. Fuchs, G. Rignanese, L. Sindic, M. Verstraete, G. Zerah, F. Jollet, et al., First-principles computation of material properties: the ABINIT software project, Comput. Mater. Sci. 25 (2002) 478–492.
[43] X. Gonze, A brief introduction to the ABINIT software package, Z. Kristallogr. 220 (2005) 558–562.
[44] G. Kresse, J. Furthuller, Efficiency of ab initio total energy calculations for metals and semiconductors using a plane-wave basis set, Comput. Mater. Sci. 6 (1996) 15–50.
[45] G. Kresse, J. Furthuller, Efficient iterative schemes for ab initio total-energy calculations using a plane-wave basis set, Phys. Rev. B 54 (1996) 11169–11186.
[46] K. Schwarz, P. Blaha, G.K.H. Madsen, Electronic structure calculations of solids using the WIEN2k package for material sciences, Comput. Phys. Commun. 147 (2002) 71–76.
[47] K. Schwarz, P. Blaha, Solid state calculations using WIEN2k, Comput. Mater. Sci. 28 (2003) 259–273.
[48] K. Dewhurst, S. Sharma, et al., The elk fp-lapw code. <http://elk.sourceforge.net/>.
[49] V. Luaña, A. Martín Pendás, J.M. Recio, E. Francisco, M. Bermejo, Quantum mechanical cluster calculations of ionic materials: the ab initio perturbed ion (version 7) program, Comput. Phys. Commun. 77 (1993) 107–134.
[50] A. Kokalj, XCrySDena new program for displaying crystalline structures and electron densities, J. Molec. Graph. Mod. 17 (1999) 176–179.
[51] M.A. Spackman, E.N. Maslen, Chemical properties from the promolecule, J. Phys. Chem. 90 (1986) 2020–2027.
[52] A. Martín Pendás, V. Luaña, L. Pueyo, E. Francisco, P. Mori-Sánchez, Hirshfeld surfaces as approximations to interatomic surfaces, J. Chem. Phys. 117 (2002) 1017–1023.
[53] J. Contreras-García, E.R. Johnson, W. Yang, Analysis of hydrogen-bond interaction potentials from the electron density: integration of noncovalent interaction regions, J. Phys. Chem. A 115 (2011) 12983–12990.
[54] Y.V. Nelyubina, M.Y. Antipin, K.A. Lyssenko, Anionanion interactions: their nature, energy and role in crystal formation, Russ. Chem. Rev. 79 (2010) 167–187.
[55] L. Glasser, H.D.B. Jenkins, Predictive thermodynamics for condensed phases, Chem. Soc. Rev. 34 (2005) 866–874.
[56] P. Coppens, Electron density from X-Ray diffraction, Annu. Rev. Phys. Chem. 43 (1992) 663–692.
[57] X. Krokidis, S. Noury, B. Silvi, Characterization of elementary chemical processes by catastrophe theory, J. Phys. Chem. A 101 (1997) 7277–7282.
[58] J.A. Wasastjerna, On the radii of ions, Soc. Sci. Fenn. Comment. Phys.-Math. 38 (1923) 1–25.
[59] L. Pauling, The sizes of ions and the structure of ionic crystals, J. Am. Chem. Soc. 49 (1927) 765–790.